A Strategy to Improve the GOES-R Land Surface Temperature Product with All Weather Information in Near Real Time

Anand K Inamdar[1]

[1]CISESS

November 28, 2022

Abstract

LST is routinely retrieved from the GOES-R Advanced Baseline Imager (ABI) long wave spectral channels. Since the product is available only under clear sky conditions, large gaps exist in the data stream which correspond to contamination by clouds. However, continuous estimates of LST data are still vitally needed for several applications such as drought monitoring ,vegetation growth, and crop yield estimation etc. Studies have shown that LST tracks with corresponding changes in incident solar radiation or more specifically changes in surface absorbed solar radiation with good correlation irrespective of sky conditions (clear or cloudy). In the present study, a scheme is developed to fill in the large spatio-temporal gaps in the LST time series using surface solar absorption parameter (SSA) retrieved in near real time from other satellites. Validation of retrieved LST values over all of the SURFRAD stations reveal RMS errors of less than 1 K.

A Strategy to Improve the GOES-R Land Surface Temperature Product with All-weather Information in Near Real Time

Anand K. Inamdar

North Carolina Institute of Climate Sciences, Asheville

Abstract

LST is routinely retrieved from the GOES-R Advanced Baseline Imager (ABI) long wave spectral channels. Since the product is available only under clear sky conditions, large gaps exist in the data stream which correspond to contamination by clouds. However, continuous estimates of LST data are still vitally needed for several applications such as drought monitoring ,vegetation growth, and crop yield estimation etc. Studies have shown that LST tracks with corresponding changes in incident solar radiation or more specifically changes in surface absorbed solar radiation with good correlation irrespective of sky conditions (clear or cloudy). In the present study, a scheme is developed to fill in the large spatio-temporal gaps in the LST time series using surface solar absorption parameter (SSA) retrieved in near real time from other satellites. Validation of retrieved LST values over all of the SURFRAD stations reveal RMS errors of less than 1 K.

1. Introduction

Land surface temperature (LST) has been recognized as an essential climate variable (ECV) by the Global Climate Observing System (GCOS) due to its importance in hydrology, meteorology and climatology. LST and its diurnal variability are key to understanding of land-atmosphere interactions, including the exchange of water and energy at the surface (Mannstein, 1987), climate change (Hansen et al. 1995), and hydrological processes. As a result, LST has been used in numerous applications (Kerr, 2000) from modeling and land cover change studies to applications in geology and epidemiology. However, many of these studies are reliant upon satellite measurements due to limited spatial coverage of in situ networks (Li et al., 2013).

Satellite retrievals of LST are available from a variety of polar orbiting and geostationary sensors. Bulk of the methods are based on a combination of thermal infrared channels and other ancillary parameters like water vapor. The new generation of advanced geostationary satellites such as GOES-R, GOES-S (US), HIMAWARI series (Japan) are providing reasonable estimates of global LST under clear sky conditions. However the presence of clouds limit the quantity and quality of remotely sensed LST measurements. To date, there have been very few studies on the retrieval of LST under cloudy skies. Jin (2000) proposed a spatial neighboring pixel approach to estimate LST under cloudy skies from polar-orbiting satellites. A drawback of this approach was sacrificing the homogeneity in the surrounding pixels. Lu et al (2011) employed a temporal neighboring pixel approach by taking advantage of the expanded temporal domain offered by geostationary satellites. However, these studies were based on a surface energy balance approach that require parameterization of surface fluxes, which are not readily available. While microwave sensors can measure LST under clouds, their spatial resolution is too course and overly sensitive to surface roughness and moisture and thus have limited applicability. Zhang et al (2015) developed a method to obtain LST under clouds based on a one-dimensional diffusion equation that estimates the temporal evolution of surface temperature using net surface solar radiation. This method based on estimation of thermal inertia worked best over homogeneous bare soils. Recently Wang et al (2019) developed a technique employing solar-cloud-satellite geometry and applied it to MODIS and Landsat-8 data to derive LST under clouds obtaining an rms accuracy of 4.9 K. In the present study, we attempt to extend the analysis of surface energy balance approach (Zhang et al 2015) to heterogenous land-cover by incorporating time series of LST retrieved under clear skies, and the diurnal cycle of surface solar absorption (SSA) observed from Geostationary Satellites (Inamdar & Guillevic 2015 – hereafter refered to as IG15) under all sky conditions.

2. Input Data

Satellite

1) GOES-R Visible channel scaled radiance counts from Level 1B data.
2) CERES: TOA broadband SW flux from the Flashflux Single Scanner Footprint (SSF) data (https://ceres-tool.larc.nasa.gov/ord-tool/products?CERESProducts=FLASH_SSF)

Ancillary

1) MODIS precipitable water from the 5-min 5 km swath data (MOD05/MYD05)

2) MODIS Aerosol Optical Depths (MOD08/MYD08)

Table 1. List of in situ stations used in this study.

Station ID	Name	State	Network	Latitude	Longitude
SGP	Southern Great Plains	OK	SURFRAD	36.60	- 97.48
DRA	Desert Rock	NV	SURFRAD	36.62	- 116.01
BOS	Table Mountain	CO	SURFRAD	40.12	-105.23
BON	Bondville	IL	SURFRAD	40.05	-88.37
FPK	Fort Peck	MT	SURFRAD	48.30	-105.10
SXF	Sioux Falls	SD	SURFRAD	43.73	-96.62
GCR	Goodwin Creek	MS	SURFRAD	34.25	-89.87
PSU	Penn. State	PA	SURFRAD	40.72	-77.93

3. Methodology

Methodology consists of mainly three primary steps: (1) the estimation of TOA broadband SW radiation through matching up GOES-R pixels with CERES footprint in near real-time, (2) the computation of surface net SW radiation or SSA from TOA SW flux through applying the CERES TOA-to-surface algorithms (IG15 study), and (3) employing the strong correlation between the SSA and LST to fill in LST values for missing or cloud-contaminated scenes. Details are provided below:

3.1 *TOA Broadband SW Flux*

GOES-R data files provide scaled radiance counts (not raw counts) at half km resolution from which channel 2 radiance can be derived using a scaling factor and offset provided in the nectddf file. But we will not need them here, since we will directly match up the CERES broadband SW flux with the scaled radiance counts. The broadband SW flux from GOES-R can be evaluated from the linear regression between scaled radiance counts and CERES broadband flux. The collocation criteria for the matching are similar to the ones used earlier for the IG15 study, albeit slightly tighter:

– The time difference between observation times for CERES and GOES is less than 10 minutes;

– The difference in viewing zenith angles between the two instruments is less than 10 degrees to reduce directional effects;

– The standard deviation of the radiances of GOES pixels within the bounding CERES coarser pixel is less than 10% of the domain mean value;

– The difference between the maximum and the minimum count values in the GOES domain is less than 20% of the domain mean value to avoid mixed pixels and undetected clouds.

The detailed arguments provided in the earlier study (IG15) against using the angular directional model (ADM) for radiance to flux conversion still hold for the present study. And regression is performed directly between the broadband flux and GOES-R scaled radiance counts. The key difference from the prior study is doing away with dependance on the nature of surface property as represented by the use of the Normalized Difference Vegetation Index (NDVI). In a future version of this study, it is planned to use dependency on surface reflectance in the red, blue and green band, as reported in (Wu et al 2019) to improve the accuracy.

3.2 *TOA to Surface Algorithm*

We employ the same model described before (IG15), namely "SW Model A" in the CERES processing chain to estimate the fraction of absorbed solar radiation. The model is based on detailed radiative transfer calculations (Li et al 1993) and requires additional ancillary inputs of column precipitable water, aerosol optical depth and cosine of solar zenith angle. Precipitable water has been retrieved by combining data from both Terra (MOD05) and Aqua (MYD05) platforms and interpolated to produce 0.05 deg lat/lon grid at GOES-R observational times. For aerosol optical we used the monthly average deep blue aerosol optical depth for land at 0.55 micron from both Terra and Aqua and used an average value.

3.3 Filling in Missing LST Values

Diurnal evolution of LST is driven by the changes in the incoming solar radiation or SSA parameter triggered by changes in insolation due to clouds (Zhang et al 2015). Studies have revealed (see figures in section 4.2) that changes in LST are linearly correlated with changes in the SSA parameter irrespective of sky conditions. We split the diurnal range of variations into an ascending leg (sunrise to time of maximum LST) and a descending leg (time of peak LST to near sunset).

4. Results and Discussion

4.1 TOA Outgoing Shortwave Radiation from GOES-R

The relationship between the outgoing CERES-measured SW radiation and aggregated GOES-R visible channel scaled radiance counts has been calibrated using matched observations as described in the previous section under all-sky conditions. The relationship between the two variables is very strongly correlated. Throughout the present study, the strength of correlation between a pair of variables is represented by the Pearson's correlation coefficient (***R***) expressed as the covariance between the two variables divided by the product of their standard deviations. Higher value closer to 1 represents a strong positive correlation and a value closer to -1 represents a strong negative correlation. Correlation between the GOES-R visible channel scaled radiance counts and the collocated CERES SW radiation over the CONUS domain (not shown) is characterized by a very high ***R*** value close to 1.

4.2 *Validation of SSA*

SSA values have been retrieved from TOA broadband SW flux as outlined before. The accuracy of the SSA parameter retrieved has been evaluated (fig. 1 – 2 and table 2) against surface measurements from radiometers at all eight SURFRAD sites for Nov 2019. Figs 1 and 2 show the time series of SSA on the top panel for a ten-day period during the month for Bondville (IL) and Goodwyn Creek (MS) sites. The continuous dark lines represent the in situ measurements while the magenta-colored diamond symbols refer to the values calculated from the model. The bottom panels depict scatter plots of pairs of values shown in the top panel, but for all the days during the month. The mean RMS error for all sites is less than 50 W m^{-2}. The error statistics are comparable or sometimes even better than those of IG15 study for all sites, in spite of the simplified treatment to derive the TOA SW radiation.

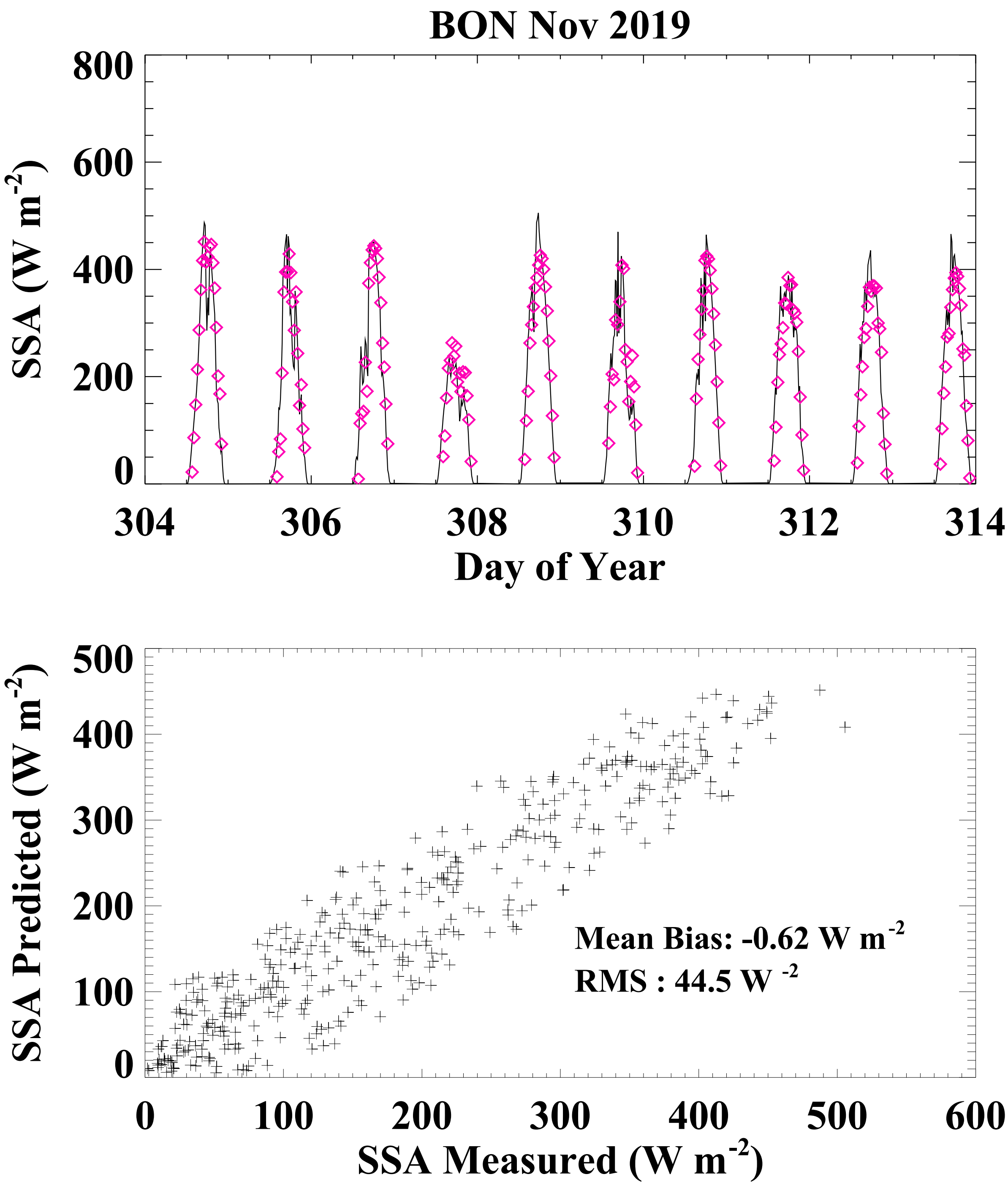

Fig 1. Top: Time series of in situ measured SSA (Wm^{-2}) (solid dark line) and modeled (predicted) SSA (magenta diamond symbols) for Bondville site (IL) for part of Nov 2019.

Abscissa units are day of year in UTC format. Bottom: Scatter plot of measured versus predicted SSA (W m^{-2}) utilizing data for all days of the month.

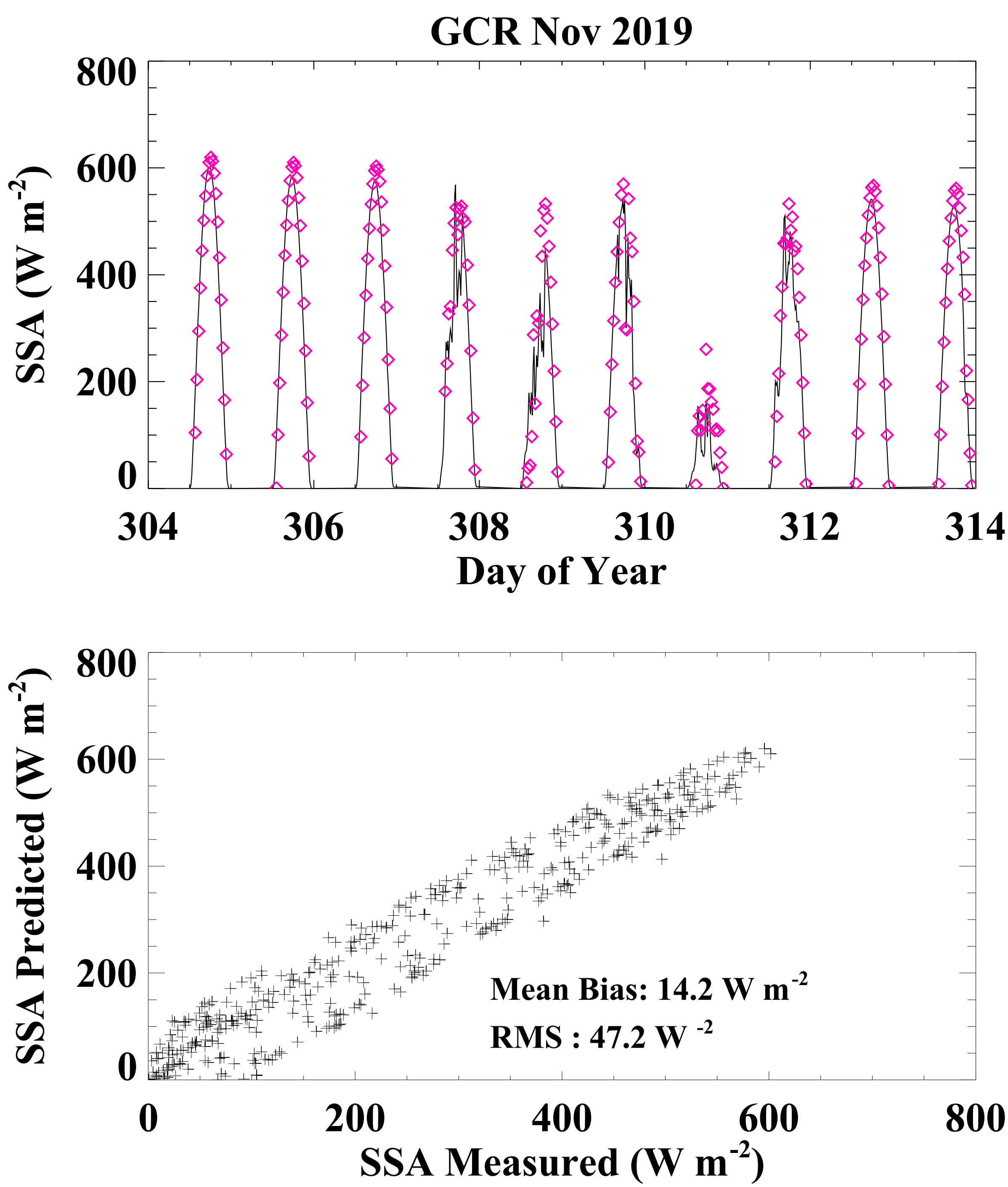

Fig 2. Same as Fig 2, but for the Goodwyn Creek (MS) site

Table 2. Summary of mean error statistics for SSA (mean bias and RMS) for the month of Nov 2019 for all SURFRAD sites

Station ID	Mean Bias (Predicted-Measured W m^{-2})	RMS (W m^{-2})
SGP	-3.7	46
DRA	-5.6	46.6
BOS	1.6	51.2
BON	-0.6	44.5
SXF	-4.5	47.8
FPK	-16.4	44.2
GCR	13.3	47.2
PSU	20.4	41.4

4.3 *SSA – LST Correlation*

A sampling of 4 sites (SGP, BOS, SXF and FPK) with day-time variations in LST for specific days of the month have been chosen to demonstrate the strong coupling between SSA and LST changes. There are 2 panels for each site and the top panel of each marked (**a,b,c,d**) shows the time series of in-situ measurements of LST. The bottom panels show the correlations between the in-situ LST and corresponding modeled SSA values split into the ascending (black symbols) and descending (magenta symbols) domains. The corresponding solid lines for each are the mean regression fit lines which will be used to fill in the missing LST slots. The two pairs of inset numbers in the each bottom panel represent the mean Pearson's correlation coefficient (***R***) as described in section 4.1, and the rms error for the filled LST series. Specifically, days with challenging situations characterized by diurnal LST variability due to presence of clouds as shown by the time series of in situ LST have been chosen for demonstration. However, correlation has been performed for all days in the month and the mean ***R*** and rms error have been tabulated in table 3 for each of the 8 SURFRAD sites. It is observed that the correlations are in the high range above 0.8 for most stations for both ascending and descending branch and the mean rms errors are also below about 1 K.

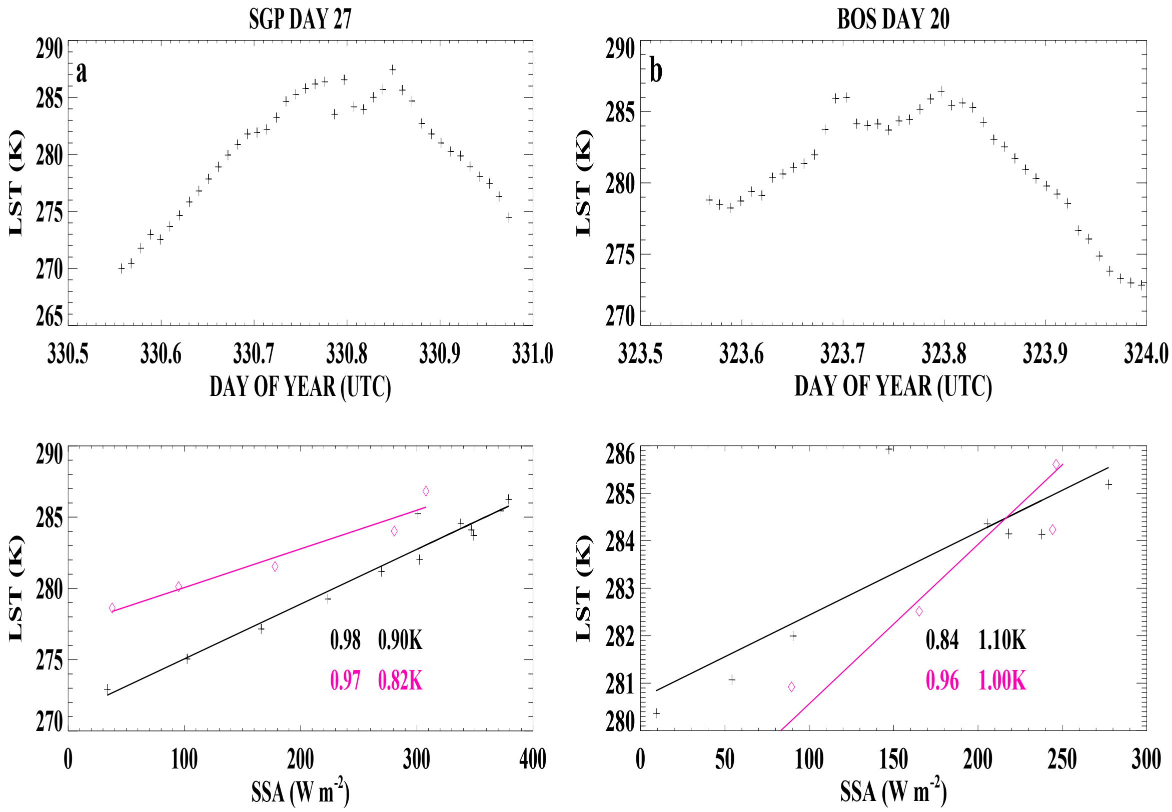
SGP DAY 27
BOS DAY 20
a
b
LST (K)
DAY OF YEAR (UTC)
SSA (W m^{-2})
0.98 0.90K
0.97 0.82K
0.84 1.10K
0.96 1.00K

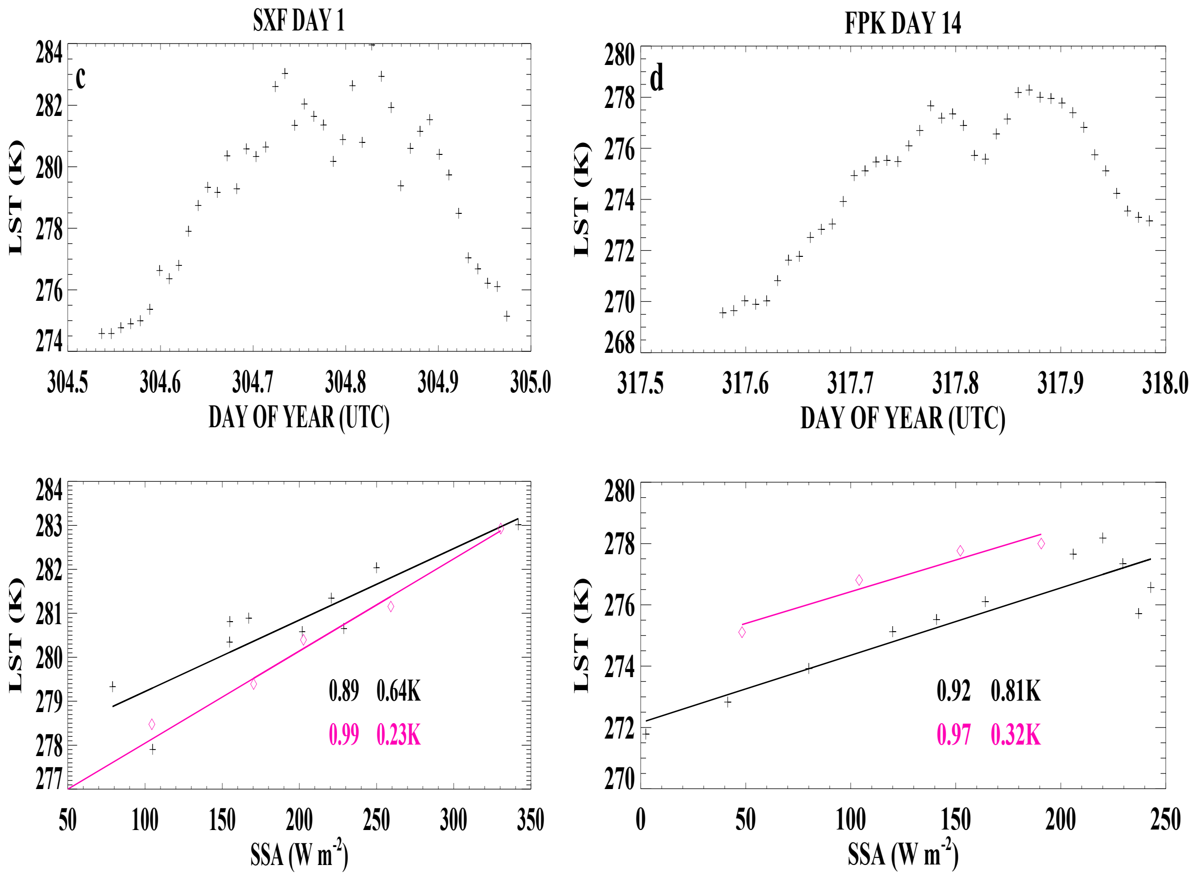

Fig 3. Top panel of each figure (a,b,c,d) shows in situ LST (K) for the specified site and day marked at the top. Bottom panels of each (a,b,c,d) shows correlation between SSA and LST for each of the ascending (sunrise to peak LST of day in dark line) and descending (time of peak LST to near sunset hour in magenta line). The symbols are the in situ measurements and continuous lines represent mean linear regression fits. Pairs of numbers inset refer to the Pearson's correlation coefficient and RMS error for each of the ascending and descending legs.

Table 3. Mean Pearson's correlation coefficient between modeled SSA and LST for ascending (ASC) and descending (DSC) legs using data for all days in the month. The corresponding mean error statistics (RMS) of regression fits are also shown in the last 2 columns.

Station ID	R (ASC)	R(DSC)	RMS (ASC) (K)	RMS (DSC) (K)
SGP	0.94	0.96	0.67	0.49
DRA	0.99	0.97	0.72	0.53
BOS	0.79	0.86	1.04	1.35
BON	0.89	0.88	1.06	0.77
SXF	0.91	0.84	0.8	0.58
FPK	0.83	0.9	0.84	0.41
GCR	0.94	0.91	0.72	0.83
PSU	0.9	0.89	0.77	0.56

5. Conclusions

In the present study we have developed a possible strategy to enhance the operational GOES-R LST product including the all-weather conditions. The strategy relies on the strong coupling between the surface absorbed solar radiation and changes in LST. The study makes use of an algorithm (IG15) designed and developed earlier to retrieve SSA from the single narrowband visible channel of GOES-8 and GOES-10 satellites and extends the approach to the current GOES-R. Since GOES-R has many additional channels than its predecessor, it is possible to further improve the accuracy of LSTs through adding other channels. Further research will also explore to enhance the accuracy of the TOA broadband flux from geostationary platforms through including surface reflectance from MODIS channels. This approach can be extended to all of the current generation of geostationary satellites such as the HIMWARI and METEOSAT third generation (MTG) series satellites.

Acknowledgements: This work was supported by NOAA through the Cooperative Institute for Satellite Earth System Studies (CISESS) - North Carolina under Cooperative Agreement NA19NES4320002. The ARM/SGP and SURFRAD data were obtained from the ARM/SGP web site (https://adc.arm.gov/discovery/#/results/meas_category_code::radio) and ftp://aftp.cmdl.noaa.gov/data/radiation/surfrad/ respectively. The CERES/FLASHFLUX data was obtained through https://ceres-tool.larc.nasa.gov/ord-tool/products?CERESProducts=FLASH_SSF. Authors are grateful for constructive comments provided by the internal reviewers at NOAA which helped a great deal in improving the quality of presentation.

References

Augustine, J. A.; Deluisi, J. J.; Long, C. N. SURFRAD — A national surface radiation budget network for atmospheric research, *Bull. Amer. Meteor. Soc.*, 2000, 81, 2341–2357.

Diamond, H. J., T. R. Karl, M. A. Palecki, C. B. Baker, J. E. Bell, R. D. Leeper, D. R. Easterling, J. H. Lawrimore, T. P. Meyers, M. R. Helfert, G. Goodge, and P. W. Thorne, 2013: U.S. Climate Reference Network after one decade of operations: status and assessment. *Bull. Amer. Meteor. Soc.,* 94, 489-498. doi: 10.1175/BAMS-D-12-00170.1

Hansen, J., M. Sato, and R. Ruedy, 1995: Long-term changes of the diurnal temperature cycle: Implications about mechanisms of global climate change. *Atmos. Res.*, **37**, 175-209, doi:10.1016/0169-8095(94)00077-Q.

Inamdar A. K. and P. C. Guillevic. Net Surface Shortwave Radiation from GOES Imagery—Product Evaluation Using Ground-Based Measurements from SURFRAD. *Remote Sensing*. 2015; 7(8):10788-10814. doi:10.3390/rs70810788

Kratz, D. P., P. W. Stackhouse, S. K. Gupta, A. C. Wilbur, P. Sawaengphokhai, and G. R. McGarragh, 2014: The fat longwave and shortwave flux (FLASHFlux) data product: single-scanner footprint fluxes., *J. Appl. Meteor. Climatol*, pp. 1059-1079. DOI: https://doi.org/10.1175/JAMC-D-13-061.1

Li, Z.; Leighton, H.G.; Cess, R.D. Surface net solar radiation estimated from satellite measurements: Comparisons with tower observations. *J. Clim.* **1993**, *6*, 1764–1772.

Li, Z., B. Tang, H. Wu, H. Ren, G. Yan, Z. Wan, I. F. Trigo, J. A. Sobrino, 2003: Satellite-derived land surface temperature: Current status and perspectives, *Remote Sens. Environ*, **131**, 14-37, https://doi.org/10.1016/j.rse.2012.12.008

Lu, L.; Venus, V.; Skidmore, A.; Wang, T.; Luo, G. Estimating land-surface temperature under clouds using MSG/SEVIRI Observations. *Int. J. Appl. Earth Obs.* **2011**, *13*, 265–276.

Mannstein H. (1987) Surface Energy Budget, Surface Temperature and Thermal Inertia. In: Vaughan R.A. (eds) Remote Sensing Applications in Meteorology and Climatology. NATO ASI Series (Series C: Mathematical and Physical Sciences), vol 201. Springer, Dordrecht

Menglin Jin, and R. E. Dickinson, A generalized algorithm for retrieving cloudy sky skin temperature from satellite thermal infrared radiances. *J. Geophys. Res*., 105, 27037 – 27047, 2000.

Safieddine, S., A. C. Parracho, M. George and others, Artificial Neural Networks to retrieve land and sea skin temperature from IASI. Remote Sens., 12, 2777. doi:10.3390/rs12172777, 2020.

Zhao-Liang Li, Bo-Hui Tang, Hua Wu, Huazhong Ren, Guangjian Yan, Zhengming Wan, Isabel F. Trigo, José A.Sobrino, Satellite-derived land surface temperature: Current status and perspectives, *Remote Sensing of Environment*, Volume 131, 2013, pp. 14-37

Y.H. Kerr, J.P. Lagouarde, F. Nerry, C. Ottle, Land surface temperature retrieval techniques and applications, D.A. Quattrochi, J.C. Luvall (Eds.), Thermal remote sensing in land surface processes, CRC Press, Boca Raton, Fla. (2000), pp. 33-109

Wang, T., S. Jiancheng, M. Ya, H. Letu, C. Edward, J. Dabin, Z. Tianjie, and X. Chuan, Recovering land surface temperature under cloudy skies considering the solar-cloud-satellite geometry: Application to MODIS and Landsat-8 data, J. Geophys. Res., 124, 3401-3416, doi: /10.1029/2018JD028976 2019.

Wu, H. and W. Ying. Benchmarking machine learning algorithms for instantaneous net surface shortwave radiation retrieval using remote sensing data. *Remote Sensing*. 2019, 11, 2520 – 2540, doi:10.3390/rs11212520.

Zhang, X., J. Pang, and L. Li, Estimation of Land Surface Temperature under Cloudy Skies Using Combined Diurnal Solar Radiation and Surface Temperature Evolution, *Remote Sens.* **2015**, *7*(1), 905-921; doi:10.3390/rs70100905